Modeling of flash sintering of ionic ceramics

K.S.N. Vikrant, X.L. Phuah, J. Lund, Han Wang, C.S. Hellberg, N. Bernstein, W. Rheinheimer, C.M. Bishop, H. Wang, and R.E. García*

K.S.N. Vikrant, Oak Ridge National Laboratory, USA; k.s.n.vikrant@gmail.com

X.L. Phuah, Purdue University, USA; xphuah@purdue.edu

J. Lund, Purdue University, USA; lund3@purdue.edu

Han Wang, Pacific Northwest National Laboratory, USA; han.wang@pnnl.gov

C.S. Hellberg, US Naval Research Laboratory, USA; steve.hellberg@nrl.navy.mil

N. Bernstein, US Naval Research Laboratory, USA; noam.bernstein@nrl.navy.mil

W. Rheinheimer, German Research Foundation, Germany; need email address

C.M. Bishop, University of Canterbury, New Zealand; catherine.bishop@canterbury.ac.nz

H. Wang, Purdue University, USA; hwang00@purdue.edu

R.E. García, Purdue University, USA; redwing@purdue.edu

A fundamental understanding of the influence of defects in ionic ceramics at the atomic, microstructural, and macroscopic levels, before, during, and after the flash sintering event is key to the development of ceramic processing operations that lead to fast, low cost, and environmentally safe fabrication of materials. The observed phenomenology of the flash process encompasses multiple time and length scales and have resulted on a wide variety of what sometimes appears to be contradictory explanations. This article summarizes the latest developments on the modeling and simulation of flash sintering, specifically those related to the understanding of the equilibrium and kinetic properties and the corresponding

microstructural evolution of ionic ceramics. Challenges and opportunities in the development of theoretical analyses that include unidentified multiphysical effects are discussed, as they pertain to the processing of technologically relevant ceramic materials for advanced structures and devices.

Keywords: point defects; charged interfaces; space charge; mechanisms of flash sintering; microstructural modeling

Introduction

The fabrication of high-performance material properties in ionic ceramics for applications such as biomedical and high-temperature structural systems, for energy storage, conversion, or electronic devices has been possible by the successful development of advanced processing techniques. One such emerging technique is flash sintering, which has been found to be environmentally friendly,[1–5] and promises to improve economic and energetic costs.[2] The development of an optimal flash sintering process requires a fundamental understanding of the microstructural mechanisms controlling the kinetics that result from the multiphysical interactions of the underlying charged point defects with surfaces and interfaces. The knowledge gaps in the understanding of the fundamentals of flash sintering have not been addressed until the recent rationalization of the atomistic mechanisms and the coupling of these mechanisms with the microstructural and macroscopic phenomena.

It is well recognized that the flash sintering process has three stages: (1) incubation kinetics, (2) the flash event, and (3) coarsening kinetics.[**Error! Bookmark not defined.**,**Error! Bookmark not defined.**,6–18] While all three stages are important in specifying the properties and resultant microstructure of the sintered material, the emphasis has been placed on describing the incubation and coarsening kinetics,[**Error! Bookmark not defined.**,**Error! Bookmark not defined.**,**Error! Bookmark not defined.**,**Error! Bookmark not defined.**,**Error! Bookmark not defined.**,**Error! Bookmark not defined.**,**Error! Bookmark not defined.**] on inferring the physics of the flash event from imaging the microstructure,[**Error! Bookmark not defined.**,**Error! Bookmark not defined.**–21] and the effects on the macroscopic properties,[**Error! Bookmark not defined.**,**Error! Bookmark not defined.**–**Error! Bookmark not defined.**,**Error! Bookmark not defined.**,**Error! Bookmark not defined.**] before and after the flash event.

In this article, we reviewed the most recent modeling and simulation efforts of the flash sintering process at different length scales, including atomistic, mesoscopic, and macroscopic, as the material transitions from the incubation stage, (1), to the coarsening stage, (3). Existing and emerging grand modeling challenges are discussed, followed by proposed future opportunities to control the processing of advanced ceramics and their underlying macroscopic properties.

The atomic scale

A wide variety of atomistic mechanisms have been proposed to describe the origins of the flash event. Raj et al. suggested that Frenkel defects (vacancy-interstitial pairs) are generated during the flash event, inducing a cascade of mass transport during the coarsening and densification process.[22] Naik and co-authors suggested that the large dielectric constant difference between grains and grain boundaries contributes to an inhomogeneous dipolar energy density that would nucleate Frenkel pairs at interfaces which, as a result, would act as Joule heating spots.[23]

Lebrun and coworkers performed *in situ* x-ray diffraction of 3YSZ during flash sintering and showed an asymmetric expansion of the lattice constants that could not be explained by Joule heating alone.[24] In these measurements, the tetragonal *a*-lattice constant increased significantly more than the *c*-lattice constant. Density functional calculations (DFT) showed that Frenkel pairs could explain this asymmetry in the expansion: cation Frenkel pairs cause the *c*-lattice constant to expand more than the *a*-lattice constant, while the opposite asymmetry occurs in calculations of oxygen Frenkel pairs. DFT calculations also showed that formation energies of the cation Frenkel defects greatly exceeds that of the oxygen Frenkel defects that form at much higher densities, and the overall calculated expansion asymmetry agrees with the experimental asymmetry.[25]

Direct formation of Frenkel pairs by the application of an electric field in the range of 100V/cm in flash sintering is implausible. Using HfO_2 as a model material, Schie and co-authors predicted 10GV/m to be required to generate Frenkel pairs in ionic ceramics.[26] However, the electroluminescence observed

during flash indicates that defect states are generated with accessible levels in the band gap of the material,[6] suggesting a set of energy states that become available during the flash event. Jo and Raj showed that while YSZ is predominantly an ionic conductor, its electronic conductivity increases dramatically at the onset of flash in cubic zirconia.[27] DFT calculations of the charged defect levels in YSZ showed that the injected carriers reduce the defect formation energies, and could drive the formation energies negative.[21] Results suggest that the reduction of defect formation energies by nonequilibrium electron and hole distributions is common to many insulators and semiconductors, which would provide an additional tentative argument to explain the avalanche of defects observed during the flash event.[21,25]

The mesoscopic scale: Equilibrium

At the mesoscopic level, the description of the microstructural properties that control the flash event has been pioneered by Vikrant and co-authors,[28] by defining a free energy formulation, F, of an ionic ceramic with energetic contributions to the different microstructural regions, $\{\eta_i\} = \{\eta_\times, \eta_d, \eta_v\}$, and N chemical species, $\left\{\left[V_j^{Z_j}\right]\right\} = \left\{\left[V_1^{Z_1}\right], \ldots, \left[V_N^{Z_N}\right]\right\}$, as the sum of contributions from thermal, chemical, electrical and elastic volumetric free energy densities, plus the chemical and structural contributions to the interfacial free energy of the granular system:**Error! Bookmark not defined.**–30

$$\begin{aligned} F[\{\eta_i\},\{[V_j^{Z_j}]\},\theta,\rho,\phi,\vec{u};T] \quad = \quad & \int_\Omega [f(\eta_\times,\eta_d,\eta_v,[V_1^{Z_1}],\ldots,[V_N^{Z_N}],T) \\ & + \tfrac{\alpha_\times^2}{2}(\nabla\eta_\times)^2 + \tfrac{\alpha_d^2}{2}(\nabla\eta_d)^2 + \tfrac{\alpha_v^2}{2}(\nabla\eta_v)^2 \\ & + g(\eta_\times)\left(s_1|\nabla\theta| + \tfrac{s_2}{2}\left|\nabla\theta\right|^2\right) + \rho\phi - \tfrac{\epsilon}{2}(\nabla\phi)^2 + \tfrac{1}{2}\overleftrightarrow{\sigma}\cdot\overleftrightarrow{\varepsilon_e}\,]d\Omega \end{aligned} \qquad (1)$$

Here, f is the Helmholtz free energy per unit volume, $\eta_\times$ is the solid crystalline lattice order parameter, η_d is the structurally disordered parameter, η_v is the open and closed porosity order parameter, θ is the crystallographic orientation order parameter represents in each single crystal grain in a two-dimensional polycrystalline material, $\vec{u}$ is the displacement field vector, $\alpha_\times$ is the gradient energy coefficient of order–disorder interface, α_d is the gradient energy coefficient of disorder-porous interface, α_v is the gradient energy coefficient of

porous–order interface, $\rho = \sum_{i=1}^{N} eZ_i[V_i^{Z_i}]$ is the electrostatic charge per unit volume, ϕ is the local electrostatic potential, ϵ is the dielectric constant, $\overleftrightarrow{\sigma}$ is the stress tensor, $\overleftrightarrow{\varepsilon_e}$ is the elastic strain tensor, $g(\eta_\times) = \eta_\times^2$ is a coupling function, and s_1 and s_2 are structural coupling parameters, as presented by Kobayashi, Warren, and Carter.[31]

The generalized equilibrium conditions of an ionic solid are a result of minimizing **Equation 1**:

$$\begin{aligned}
\frac{\delta F}{\delta \theta} &= -g(\eta_\times)(s_1 \nabla \cdot [\tfrac{\nabla\theta}{|\nabla\theta|}] + s_2 \nabla^2 \theta) \\
\frac{\delta F}{\delta \eta_\times} &= \frac{\partial f}{\partial \eta_\times} - \alpha_\times^2 \nabla^2 \eta_\times - \frac{\alpha_d^2}{2}\nabla^2\eta_v + \frac{\partial g}{\partial \eta_\times}(s_1|\nabla\theta| + \tfrac{s_2}{2}|\nabla\theta|^2) \\
\frac{\delta F}{\delta \eta_v} &= \frac{\partial f}{\partial \eta_v} - \alpha_v^2 \nabla^2 \eta_v - \frac{\alpha_d^2}{2}\nabla^2\eta_\times \\
\frac{\delta F}{\delta [V_i^{Z_i}]} &= \xi_i = \frac{\partial f}{\partial [V_i^{Z_i}]} + Z_i e\phi - \overrightarrow{\beta} \cdot \overrightarrow{\sigma} \\
\frac{\delta F}{\delta u_i} &= \nabla \cdot \overrightarrow{\sigma} = \overrightarrow{0} \\
\frac{\delta F}{\delta \phi} &= \nabla \cdot \epsilon \nabla \phi + \rho = 0
\end{aligned} \qquad (2)$$

Site conservation, $\eta_\times + \eta_d + \eta_v = 1$, is imposed on the system. $\eta_d = 1 - \eta_\times - \eta_v$ has been substituted in **Equation 2**.

Equation 2 defines the coarse-grained mesoscale structural state of the ceramic material, including the volumetric, interfacial particle-particle contacts, and particle-surface contacts contributions (first three rows).**Error! Bookmark not defined.**–**Error! Bookmark not defined.** The electro-chemo-mechanical potential, ξ_i, (the fourth row) defines the local driving force for mass and charge accumulation of the *i*-th chemical species at particle-particle and particle-surface contacts due to local structural, chemical, electrical, and mechanical stress inhomogeneities.**Error! Bookmark not defined.**,**Error! Bookmark not defined.**,[32–34] Together with the mechanical equilibrium equation (fifth row),**Error! Bookmark not defined.**,[35,36] and Coulomb's equation in its differential form (last row),**Error! Bookmark not defined.**–**Error! Bookmark not defined.**,**Error! Bookmark not defined.**,**Error! Bookmark not defined.** Equation 2 naturally enables the thermodynamically consistent description of charged interfaces in ionic ceramics in the strong and dilute solution limit. In particular, Equations 1 and 2 reduce to the classical description of interfaces, including Debye (D) and Mott–Schottky (MS) type,**Error! Bookmark not defined.**,**Error! Bookmark not**

defined. in the dilute solution limit. As compared to classic models, such as Gouy–Chapman,[37,38] Debye–Hückel,[39] Mott–Schottky,[40,41] and others,[42] Equation 2 is a unique starting point to describe the generality of formation, equilibrium, and phase transitions, at grain boundaries and interfaces, induced by multiphysical fields such as externally applied mechanical stresses, electrical fields, crystallographic misorientations, and chemical and thermal stimuli,**Error! Bookmark not defined.**,**Error! Bookmark not defined.** filling an important gap on the description of the effects of the electrochemical interfaces on the macroscopic transport properties, as they have been highlighted by more than 30 years of research.[43–49] This has been a long-standing fundamental problem in the description of ionic and mixed conducting ceramics.**Error! Bookmark not defined.**–**Error! Bookmark not defined.**

As a direct application of the developed approach, **Figure 1** shows the prediction of charge at interface and the development of grain-boundary electrochemical phase transitions, in terms of an equilibrium orientation-composition (phase) diagram for YSZ at 2000 K. The theory highlights the structural and electrochemical character of interfaces (Figure 1a–b), and its effect on the experimentally measured transport properties, see Figure 1d.[50–52] These results highlight the complexity induced by the interfacial properties in an ionic ceramic, and constitutes a critical building block to describe the mesoscopic charge transport and Joule heating during the flash event. The successful incorporation of the underlying atomistic equilibrium point defect formation and migration energetics is key to the development of a successful multiscale description of flash sintering.Error! Bookmark not defined.,Error! Bookmark not defined.,Error! Bookmark not defined.–Error! Bookmark not defined. Further, while it is common to describe interfaces and their properties as independent of the physical characteristics of the abutting grains, including structural and crystallographic orientation differences (i.e., misorientation), this work demonstrates that the grain-boundary–grain interactions are key to explain the observed behavior,Error! Bookmark not defined.,Error! Bookmark not defined. and thus enable to understand the macroscopic properties of ionic ceramics.[53,54] For example, for 8YSZ, at a small angle misorientation, $\Delta\theta = 15^{\circ}$(see Figure 1a),

the interface is atomically sharp and reminiscent of a Debye (D)-type single charged layer with excess oxygen vacancies in the core followed by a depletion zone of oxygen vacancies and yttrium defects in the immediate neighborhood.[30] For $\Delta\theta = 30^{\circ}$(see Figure 1b), a thick grain boundary develops and favors a higher oxygen vacancy concentration at the core followed by wide depletion zone of oxygen vacancies and yttrium defects in the immediate neighborhood. The resultant positive interface attracts opposite polarity electrons, and depletes holes, defining a MS-type interface.[30] Figure 1c–d shows that structurally disordered, large angle, MS-type 8YSZ interfaces display a lower total electrical conductivity than ordered small angle, D-type interfaces due to the formation of thick space charge layers with oxygen vacancy depletion. The maximum predicted total electrical conductivity is a result of the decrease in the width of the depletion zone of oxygen vacancies in excellent agreement with experimental results.Error! Bookmark not defined.–Error! Bookmark not defined. Overall, the results summarized in Figure 1 demonstrate that the interfacial properties in ionic ceramics play an important role at specifying charge transport, as the powder compacts approach the flash event.

Experimentally, the existence of structural grain-boundary transitions is well known for many material systems.[55–59] In the particular case of phase transition of charged grain boundaries, experimental analyses should be carried out by combining transmission electron microscopy (TEM), atom probe microscopy, and impedance spectroscopy to evaluate the structural and electrochemical properties.[60,61] While difficult to fabricate, the transition in structural and electrochemical character of bicrystals under applied external fields will allow to establish correlations to the resultant interfacial properties, and thus develop a detailed understanding on the sintering/grain coarsening kinetics of different size distributions in a powder compact microstructure. Such analyses have not yet been developed and thus remain a completely wide open field.

The mesoscopic scale: Kinetics and microstructure evolution

Classic mesoscopic models to describe flash sintering includes work by Narayan and Chaim and co-workers.[62–64] Narayan proposed that the ionic mobility and

enthalpy of migration during flash sintering are affected by the local electric fields. His analytical equations aim to explain grain growth and propose that the field-induced generation of anion vacancies will preferentially segregate at dislocation loops and grain boundaries.[62] The excess of anion vacancies at the grain boundaries would result in localized Joule heating and premelting, thus purportedly leading to the onset of flash.[63] Chaim and co-workers proposed the possibility of overheating/premelting of particle-particle contacts as a mechanism to rationalize the onset of the flash event as a result of local Joule heating due to an abrupt increase in the electrical conductivity.[64] In contrast, experimental flash sintering studies on 3YSZ by Todd and co-workers emphasize that the large thermal gradients for time scales greater than ~1 μs cannot be physically justified from local Joule heating hot spots alone, due to the high thermal diffusivity of 3YSZ.**Error! Bookmark not defined.**,[65]

Most recently, the equilibrium equations describing the structural and electrochemical state of charged interfaces (see previous section) sets the stage to describe grain-boundary motion and microstructural evolution in ionic solids, as a first step to describe the flash sintering incubation kinetics and the microstructural evolution, as experimentally reported in the literature.**Error! Bookmark not defined.**,**Error! Bookmark not defined.**,**Error! Bookmark not defined.**,**Error! Bookmark not defined.**,**Error! Bookmark not defined.**

From Equations 1 and 2, the kinetic equations that naturally result are:

$$\begin{aligned}
\frac{\partial\theta}{\partial t} &= M_\theta[g(\eta_\times)(s_1\nabla\cdot[\tfrac{\nabla\theta}{|\nabla\theta|}]+s_2\nabla^2\theta)] \\
\frac{\partial\eta_\times}{\partial t} &= -M_{\eta_\times}[\tfrac{\partial f}{\partial\eta_\times}-\alpha_\times^2\nabla^2\eta_\times-\tfrac{\alpha_d^2}{2}\nabla^2\eta_v+\tfrac{\partial g}{\partial\eta}(s_1|\nabla\theta|+\tfrac{s_2}{2}\nabla\theta|^2)] \\
\frac{\partial\eta_v}{\partial t} &= \nabla\cdot M_{\eta_v}\nabla[\tfrac{\partial f}{\partial\eta_v}-\alpha_v^2\nabla^2\eta_v-\tfrac{\alpha_d^2}{2}\nabla^2\eta_\times] \\
\frac{\partial[V_i^{z_i}]}{\partial t} &= \nabla\cdot M_{\left[V_i^{z_i}\right]}\nabla[\tfrac{\partial f}{\partial\left[V_i^{z_i}\right]}+Z_i e\phi-\vec{\beta}\cdot\vec{\sigma}]
\end{aligned} \tag{3}$$

for small deviations away from equilibrium. The first three rows of **Equation 3** define the crystallographic orientation Allen–Cahn kinetics of every grain, the $\eta_\times$ to η_d transformation in the condensed phase as a nonconserved quantity, and the η_v, porous phase (i.e., the space left by the condensed ionic ceramic [a conserved quantity, described by a Cahn–Hilliard equation]).**Error! Bookmark not defined.**,**Error! Bookmark not defined.**,**Error! Bookmark not defined.** The fourth row corresponds to N Cahn–

Hilliard equations to describe the transport of charged solute and point defects.**Error! Bookmark not defined.**,**Error! Bookmark not defined.**–**Error! Bookmark not defined.** Uniquely, physical descriptions such as those summarized by Equations 2 and 3 allow to rationalize the incubation kinetics of flash sintering in ionic ceramics. Readily published results demonstrate that the orientational discontinuities at the particle-particle contacts and pore surfaces favor the accumulation of charged defects and the development of charged interfaces.[28]

The application of a macroscopic voltage difference induces local voltage deviations from equilibrium, $\delta\phi$, as described by the charge continuity equation:**Error! Bookmark not defined.**

$$\frac{\partial \rho}{\partial t} = \nabla \cdot \kappa \nabla(\delta\phi) \quad (4)$$

Here, $\kappa = \sum_{i=1}^{N} \frac{e^2 Z_i^2 \left[V_i^{Z_i}\right] D_i}{k_B T}$ is the total electrical conductivity, and $D_i = D_i^{\circ}\left[V_i^{Z_i}\right]\exp\left(-\frac{E_{a,i}}{k_B T}\right)$ is the self-diffusion coefficient with the pre-exponential constant, D_i°, and $E_{a,i}$ is the activation energy, thus inducing Joule heating in the system. The spatial dependence of the material properties is a result of solving Equations 1 to **Equation 4**.

The temperature kinetics of a flash sintered green body under an externally applied electric field with oven-imposed heating has been researched, in terms of lumped parameter (macroscopic models) descriptions.[22,66] Zhang and co-workers[7] developed a graphical construction for the heat balance between thermal and electrical runaway events to predict the temperature of the flashed sample, while Todd and co-authors[9] predicted the critical flash temperatures and applied electric fields for thermal runaway. Dong and Chen[10] put forward a heat balance equation description as a function of heating rate and removed its explicit time dependence, to predict flash temperature and activation energy of electrical resistivity for several materials.

A generalized fundamental description of the enthalpy of a volume element of material and the heat transport equation in agreement with Equations 1–4 is given by:[28]

$$c_\sigma \frac{\partial T}{\partial t} = \nabla \cdot (\lambda \nabla T) + \kappa(\nabla(\delta\phi))^2 + \Delta H^{\times \to d} \frac{\partial \eta_\times}{\partial t}, \qquad (5)$$

which includes contributions from Joule heating, heat diffusion and the local rate of change of order-disorder phase transformations. c_σ is the heat capacity per unit volume at constant stress of 1 Atm = 101 kPa, λ is the position-dependent thermal conductivity, κ is the position-dependent electrical conductivity, $\vec{E} = -\nabla\delta\phi$ is externally applied electric field, and $\Delta H^{\times \to d}$ is the latent heat of melting. Black body radiation heat exchange is imposed as an externally imposed boundary condition. The homogenization of **Equation 5** results in the lumped model:[67]

$$c_\sigma \frac{\partial \langle T \rangle}{\partial t} = \langle \kappa \rangle (\nabla \langle \delta\phi \rangle)^2 + \sigma_e e A (T_f^4 - \langle T \rangle^4) + \Delta H^{\times \to d} \frac{\partial \langle \eta_\times \rangle}{\partial t}, \qquad (6)$$

reducing to the approach proposed by Zhang et al. [7] and Todd and co-workers[9] in the absence of microstructural effects. $\langle \kappa \rangle$ is the microstructurally averaged electrical conductivity, $\nabla\langle\delta\phi\rangle$ is externally applied macroscopic electric field, σ_e is Stefan–Boltzmann constant, e is emissivity of the sintered gray body, A is the effective surface area, and $\langle T \rangle$ is the average temperature of the solid.

The application of Equations 3 to **Equation 6** to describe microstructural charge transport of a granular ceramic demonstrates a successful experiment-model comparison for the flash sintering of 3YSZ**Error! Bookmark not defined.** (see **Figure 2**), as reported in Reference 28. The underlying microstructural interactions of point defects with the particle-particle contacts and internal surfaces results in the predicted macroscopic power density response as a function of furnace temperature and time, see Figure 2a. As compared to existing formulations that only describe the atomistic,**Error! Bookmark not defined.**,**Error! Bookmark not defined.**,**Error! Bookmark not defined.** or models that only include the macroscopic aspects of the flash incubation process, this description explicitly considers the underlying microstructural features as coupled with the underlying electrochemical and structural state of particle-particle contacts and internal pore surfaces. At the microstructure level (see Figure 2b–d), results demonstrate that particle-particle contacts and triple junctions accumulate oxygen vacancies due to thermally activated chemical driving forces, which naturally attracts yttrium

defects due to its opposite charge polarity, thus establishing the correlation between the underlying microstructural response and the macroscopic behavior.

The cumulative microstructural interactions from the different particle-particle contacts and pore surfaces, including particle size and curvature effects, induce a local accumulation and depletion of yttrium (see **Figure 3**b) and oxygen vacancies (see Figure 3c) away from their average (macroscopic) concentrations. The interfaces favor charge accumulation (see green color in Figure 3b) and the development of charged solute depletion regions in the immediate neighborhood of the grain boundaries (see shades of purple in Figure 3b), consistent with the results in Figure 1c–d. Chemically, higher concentration of yttrium and oxygen vacancies at contact points and triple-junctions dominate the segregation at the interface, changing the interfaces that would favor the transport of charge. Additionally, large depleted regions are predicted in the contact areas with negative radius of curvature. Wetting and dewetting of contacting particles directly impact the position-dependent total electrical conductivity of the granular solid.

At a furnace temperature of $T_f = 1000\text{K}$ (see Figure 3d), the developed interfaces impart structural disorder, which in turn enables charge to percolate across a random distribution of granular particles (see streamlines). Overall, the contact areas, surfaces, and triple junctions with local higher electrical conductivity result in favorable charge transfer paths across tortuously connected regions. For a furnace temperature of $T_f = 1300\text{K}$ (see Figure 3e), the local wetting and electrochemical segregation of the particles increases, a large number of charge-transport paths develop, enabling the transition from oven-heated to internal, self-generated Joule heating, resulting in the thermal runaway event that we now as the flash event.[**Error! Bookmark not defined.**,**Error! Bookmark not defined.**,**Error! Bookmark not defined.**] Specifically, the calculation uniquely demonstrates that the incubation time is a result of the buildup of charge transport percolating paths, transitioning the granular system from oven-induced heating to internally induced, enabling the development of a massive topological reconfiguration, as driven by thermomechanical,[**Error! Bookmark not defined.**–**Error! Bookmark not defined.**,**Error! Bookmark not**

defined.,**Error! Bookmark not defined.** chemomechanical,**Error! Bookmark not defined.** and electrical**Error! Bookmark not defined.**,**Error! Bookmark not defined.**,**Error! Bookmark not defined.**,**Error! Bookmark not defined.**,**Error! Bookmark not defined.** driving forces as it takes over the dynamics of the system.**Error! Bookmark not defined.** The cumulative effects result in the predicted macroscopic power density response as a function of furnace temperature and time for 3YSZ samples, see Figure 1a, in excellent agreement with published experimental results.[4]

The kinetics of the flash event itself remains a completely open opportunity. Experimental results highlight that the short-lived, massive reconfiguration of the atoms is dominated by the motion of defects, as demonstrated by electroluminescence experiments.**Error! Bookmark not defined.**,**Error! Bookmark not defined.**,**Error! Bookmark not defined.**,**Error! Bookmark not defined.**–**Error! Bookmark not defined.** Simulations such as those demonstrated in[28] and highlighted in Figure 2 and Figure 3 show that the accumulation of charged solute and point defects plays a critical role, while the high density of dislocations reported after the flash event[20] suggests that plasticity in ceramics develops and controls the flash kinetics. Thus, to formally demonstrate these kinetics, a multiscale and multiphysical description will be necessary to close the gap between incubation and coarsening stages of sintering.

After the electroluminescent flash event, the kinetics of grain growth are dominated by motion of electrically charged grain boundaries. Narayan hinted at the possibility of the generality of electrical, interfacial, and osmotic driving forces to be responsible for the motion of the charged interfaces.**Error! Bookmark not defined.**,**Error! Bookmark not defined.** Vikrant and coworkers employed Equations 1 to 6 to describe grain coarsening in ionic ceramics under external chemical, mechanical, and electrical fields. The developed formulation describes the effects of charged solute distribution on grain-boundary motion.[68,69] The proposed formulation is a natural extension of existing solute drag models for metallic systems.[70–74]

As an example, **Figure 4** shows the grain coarsening kinetics of polycrystalline YSZ at 2000 K using Equation 3. Four types of charged interfaces are observed: (1) small angle misorientation grain boundaries, which are thin,

structurally ordered, and experience a low electrochemical drag force due to a negligible space charge at the interface; (2) large-angle misorientation grain boundaries, which are thick, structurally disordered interfaces and experience a large electrochemical drag force; (3) a small population of negatively charged grains; and (4) disordered regions that are electrically neutral and possess higher electrostatic potential than the corresponding single-crystal chemistry. The velocity of grain boundaries is a function grain-boundary misorientation, interfacial defect accumulation and mobility, and externally applied fields. The positive, large interfacial core charge density that develops in structurally thick grain boundaries and triple junctions, as well as the charge and solute asymmetry that develops in the vicinity of curved grain boundaries, leads to a local electrostatic potential distribution which extends across long microstructural distances, thus impacting the grain size populations. The resultant bimodal grain size microstructure is in qualitative agreement with abnormal grain growth of 8YSZ experimental results, as reported by Dong and Chen.[75]

The macroscopic scale

A set of coarse grain numerical descriptions have been developed to predict the macroscopic onset of the flash sintering, which is macroscopically determined by the electroluminescence radiated by the sample and by the rapid increase of the total electrical conductivity.[**Error! Bookmark not defined.**,**Error! Bookmark not defined.**,8,76] Raj and co-authors proposed a lumped-parameter model based on black body radiation to determine the average temperature of a sample as a function of physical dimensions, furnace temperature, and applied electrical power.[**Error! Bookmark not defined.**] Several authors developed finite element models to predict the temporal and spatial temperature distribution of a green body during flash sintering,[**Error! Bookmark not defined.**,77–80] enabling a useful understanding on the coarse-grained thermal localizations for different furnace and applied electric field conditions.[**Error! Bookmark not defined.**,**Error! Bookmark not defined.**] The observed onset of flash sintering has been rationalized using thermal runaway coarse grain models, as proposed by Zhang and co-workers for ZnO,[7] Todd and co-authors for YSZ,[9] and also Dong and Chen.[10] In these models, the temperature of the sample

increases due to the energy contributions from Joule heating and black body radiation heating from the furnace. The onset temperature of flash sintering has been determined when the radiation heating of furnace equals the Joule heating of the sample. Similarly, recent ultrafast high-temperature thermal annealing experiments on a wide variety of materials,[81] including ZnO[82] and 3YSZ,[83,84] achieved densification rates similar to those achieved in flash sintered samples indicating that the heating rate of the sample is an important controlling factor for fast densification and grain growth rates. Even though they might fall short to include the underlying microstructural and atomistic properties and do not account for the incubation kinetics of flash sintering, sample densification, and grain growth during and after flash event, some of them can reasonably reproduce the electric characteristics of flash sintering,[9] making them a great starting point for the macroscopic design of the sintering process.

Outlook for the future

The most recent efforts on the modeling and simulation of flash sintering havefocused on describing three different length scales: atomic-, meso-, and macroscales. However, even though three stages have been clearly identified to describe the flash process, modeling efforts have most recently focused on describing the incubation kinetics process alone.

At the atomic level, published research demonstrates that one single mechanism controlling the flash event is unlikely, and the quantification of the true role of Frenkel defects for nonmetallic systems will remain an active area of research. However, the prediction of relevant material properties is important to understand the atomistic mechanisms associated to the mass transport and densification process. The availability of first-principles data is the ideal starting point to develop physically consistent mesoscale and macroscale models to describe the time-dependent mass flow kinetics, densification, and grain growth during and after the flash event, particularly for systems that are locally away from equilibrium. Unfortunately, only for very few material systems, complete sets of energies of formation and migration, equilibrium, and transport property data are available to develop detailed models and thus present a comprehensive

understanding of the flash process. In this context, the accurate description of the kinetics before, during, and after the flash event will be a result of integrating mesoscopic and atomistic descriptions. In isolation, we will fall short to describe the physical process at a single length or time scale.

A wide range of unexplored modeling challenges still remain. A few of them stand out from the current review: (1) the formal demonstration of the multiscale and multiphysical kinetics of the flash event itself is necessary to close the gap between incubation and coarsening stages of sintering; (2) the thermodynamically consistent modeling of co-sintering of differing ionic ceramics to optimize the structural and electrochemical performance of interfacial phases and thus improving the interfacial phase-transport properties; (3) the modeling of the flash sintering of mixed amorphous-crystalline systems, where the defect formation energies in different phases need to be integrated with space charge and grain growth models.

The most recent work on the meso- and microstructural models set the stage to develop advanced polycrystalline ionic and mixed ionic conductor ceramics for sensors and energy applications and will provide the fundamental basis to engineer the underlying processing operation through the application of external fields such as thermal, chemical, mechanical, and electromagnetic.

Acknowledgments

The authors are grateful for the support provided by US Office of Naval Research (N00014–17–1-2087 [sintering and modeling] and N00014–20–1-2043 [TEM]). W.R. acknowledges funding from the German Science Foundation (DFG), under priority program “Fields Matter” SPP 1959 (HO 1165/20) and under the Emmy-Noether-Program (RH 146/1).

References

1. E. Comission, *Ceramic Manufacturing Industry* **19**, 210 (2007).

2. M. Biesuz, V.M. Sglavo, *J. Eur. Ceram. Soc.* **39**, 115 (2019).

3. W.-H. Tuan, J.-K. Guo, *Multiphased Ceramic Materials: Processing and Potential* (Springer, New York, 2004).

4. M. Cologna, B. Rashkova, R. Raj, *J. Am. Ceram. Soc.* **93**, 3556 (2010).

5. J.A. Downs, V.M. Sglavo, R. Raj, *J. Am. Ceram. Soc.* **96**, 1342 (2013).

6. K. Terauds, J-M. Lebrun, H-H. Lee, T-Y. Jeon, S-H. Lee, J.H. Je, R. Raj *J. Eur. Ceram. Soc.* **35**, 3195 (2015).

7. Y. Zhang, J. Il. Jung, J. Luo, *Acta Mater.* **94**, 87 (2015).

8. J.M. Lebrun, R. Raj, *J. Am. Ceram. Soc.* **97**, 2427 (2014).

9. R.I. Todd, E. Zapata-Solvas, R.S. Bonilla, T. Sneddon, P.R. Wilshaw, *J. Eur. Ceram. Soc.* **35**, 1865 (2015).

10. Y. Dong, I.W. Chen, *J. Am. Ceram. Soc.* **98**, 3624 (2015).

11. S. Grasso, Y. Sakka, N. Rrendtroff, C. Hu, G. Maizza, H. Borodianska, O. Vasylkiv, *J. Ceram. Soc. Jpn.* **119**, 144 (2011).

12. R. Baraki, S. Schwarz, O. Guillon, *J. Am. Ceram. Soc.* **95**, 75 (2012).

13. J.G.P. da Silva, H.A. Al-Qureshi, F. Kell, R. Janssen, *J. Eur. Ceram. Soc.* **36**, 1261 (2016).

14. Y. Du, A.J. Stevenson, D. Vernat, M. Diaz, D. Marinha, *J. Eur. Ceram. Soc.* **36**, 749 (2016).

15. S.K. Jha, K. Teraudus, J.-M. Lebrun, R. Raj, *J. Ceram. Soc. Jpn.* **124**, 283 (2016).

16. R. Muccillo, E.N.S. Muccillo, *J. Eur. Ceram. Soc.* **35**, 1653 (2015).

17. M. Biesuza, P. Luchi, A. Quaranta, A. Martucci, V.M. Sgalvo, *J. Eur. Ceram. Soc.* **37**, 3125 (2017).

18. K. Naik, S.K. Jha, R. Raj, *Scr. Mater.* **118**, 1 (2016).

19. S.K. Jha, H. Charalambous, H. Wang, X.L. Phuah, C. Meade, J. Okasinski, H. Wang, T. Tsakalakos, *Ceram. Int.* **44**, 15362 (2018).

20. J. Cho, J. Li, H. Wang, Z. Fan, J. Li, S. Xue, K.S.N. Vikrant, H. Wang, T.B. Holland, A.K. Mukherjee, R.E. García, X. Zhang, *Nat. Commun.* **9**, 2063 (2018).

21. H. Wang, X.L. Phuah, J. Li, T.B. Holland, K.S.N. Vikrant, L. Qiang, C.S. Hellberg, N. Bernstein, R.E. García, A.K. Mukherjee, X. Zhang, H. Wang, *Ceram. Int.* **45**, 1251 (2019).

22. R. Raj, M. Cologna, J.S.C. Francis, *J. Am. Ceram. Soc.* **94**, 1941 (2011).

23. K.S. Naik, V.M. Sglavo, R. Raj, *J. Eur. Ceram. Soc.* **34**, 4063 (2014).

24. J.-M. Lebrun, T.G. Morrissey, J.S. Francis, K.C. Seymour, W.M. Kriven, R. Raj *J. Am. Ceram. Soc.* **98**, 1493 (2015).

25. J.-M. Lebrun, C.S. Hellberg, S.K. Jha, W.M. Kriven, A. Stevenson, K.C. Seymour, N. Bernstein, S.C. Erwin, R. Raj *J. Am. Ceram. Soc.* **100**, 4965 (2017).

26. M. Schie, S. Menzel, J. Robertson, R. Waser, R.A. DeSouza, *Phys. Rev. Mater.* **2**, 035002 (2018).

27. S. Jo, R. Raj *Scr. Mater.* **174**, 29 (2020).

28. K.S.N. Vikrant, H. Wang, A. Jana, H. Wang, R.E. García, *npj Comput. Mater.* **6**, 1 (2020).

29. K.S.N. Vikrant, W.C. Chueh, R.E. García, *Energy Environ. Sci.* **11**, 1993 (2018).

30. K.S.N. Vikrant, R.E. García, *NPJ Comput. Mater.* **5**, 1 (2019).

31. R. Kobayashi, J.A. Warren, W.C. Carter , *Physica D* **140**, 141 (2000).

32. M. Tang, W.C. Carter, R.M. Cannon, *Phys. Rev. B Condens. Matter Mater.* **73**, 024102 (2006).

33. R.E. García, C.M. Bishop, W.C. Carter, *Acta Mater.* **52**, 11 (2004).

34. C.M. Bishop, R.E. García, W.C. Carter, *Acta Mater.* **51**, 1517 (2003).

35. F. Larché, J.W. Cahn, *Acta Metall.* **21**, 1051 (1973).

36. S. Suresh, *Fatigue of Materials* (Cambridge University Press, 1998).

37. D.L. Chapman, *Philos. Mag. J. Sci.* **25**, 475 (1913).

38. M. Gouy, *J. Phys. Théorique Appliquée.* **9**, 457 (1910).

39. P. Debye, E. Hückel, *Phys. Zeitschrift.* **24**, 185 (1923).

40. N.F. Mott, *Proc. R. Soc. A Math. Phys. Eng. Sci.* **171**, 27 (1939).

41. W. Schottky, *Zeitschrift für Phys.* **113**, 367 (1939).

42. D.S. Mebane, R.A. De Souza, *Energy Environ. Sci.* **8**, 2935 (2015).

43. J. Maier, *Prog. Solid State* **23**, 171 (1995).

44. S. Kim, J. Maier, *J. Elec. Soc.* **23**, J73 (2002).

45. X. Guo, W. Single, J. Maier, *J. Am. Ceram. Soc.* **86**, 77 (2003).

46. M. Aoki, Y.-M. Chiang, I. Kosacki, L.J.R. Lee, H.T.Y. Liu, *J. Am. Ceram. Soc.* **79**, 1169 (1996).

47. H. Yoshida, K. Yokoyama, N. Shibata, Y. Ikuhara, T. Sakura, *Acta Mater.* **52**, 2349 (2004).

48. N. Shibata, F. Oba, T. Yokoyama, Y. Ikuhara, *Philos. Mag. Lett.* **84**, 2381 (2004).

49. J. Luo, *Appl. Phys. Lett.* **95**, 071911 (2009).

50. J.M. Dixon, L.D. LaGrange, U. Merten, C.F. Miller, J.T. Porter, *J. Electrochem. Soc.* **110**, 276 (1963).

51. D.W. Strickler, W.G. Carlson, *J. Am. Ceram. Soc.* **47**, 123 (1964).

52. R.E.W. Casselton, *Phys. Status Solidi A* **2**, 571 (1970).

53. D.M. Saylor, B.S. El-Dasher, B.L. Adams, G.S. Rohrer, *Metall. Mater. Trans. A* **35**, 1981 (2004).

54. S. Ratnaphan, Y. Yoon, G.S. Rohrer, *J. Mater. Sci.* **49**, 4938 (2014).

55. S. Dillon, M. Tang, W.C. Carter, M.P. Harmer, *Acta Mater.* **55**, 6208 (2007).

56. P.R. Cantwell, M. Tang, S. Dillon, J. Luo, G.S. Rohrer, M.P. Harmer, *Acta Mater.* **62**, 1 (2014).

57. J. Luo, *Appl. Phys. Lett.* **95**, 071911 (2009).

58. J.M. Rickman, J. Luo, *Curr. Opin. Solid State Mater. Sci.* **20**, 225 (2016).

59. W. Rheinheimer, M.J. Hoffmann, *Curr. Opin. Solid State Mater. Sci.* **20**, 286 (2016).

60. W. Rheinheimer, J.P. Parras, J.-H. Preusker, R.A. De Souza, M.J. Hoffmann, *J. Am. Ceram. Soc.* **102**, 3779 (2019).

61. W. Rheinheimer, X.L. Phuah, H. Wang, F. Lemke, M.J. Hoffmann, H. Wang, *Acta Mater.* **165**, 398 (2019).

62. J. Narayan, *Scr. Mater.* **68**, 785 (2013).

63. J. Narayan, *Scr. Mater.* **69**, 107 (2013).

64. R. Chaim, G. Chevallier, A. Weibel, C. Estournés, *J. Appl. Phys.* **121**, 145103 (2017).

65. R.I. Todd, *Proc. IV Adv. Ceram. Appl. Conf.* 1 (2017).

66. S.K. Jha, X.L. Phuah, J. Luo, C.P. Grigoropoulos, H. Wang, R.E. García, B. Reeja-Jayan, *J. Am. Ceram. Soc.* **102**, 5 (2019).

67. J.L. Auriault, P. Royer, *Int. J. Heat Mass Transfer.* **36**, 2613 (1993).

68. K.S.N. Vikrant, W. Rheinheimer, R.E. García, *NPJ Comput. Mater.* Accepted (2020).

69. K.S.N. Vikrant, W. Rheinheimer, H. Sternlicht, M. Bäurer, R.E. García, *Acta Mater. Acta Mater.* **200**, 727 (2020).

70. J.W. Cahn, *Acta Matall.* **10**, 789 (1962).

71. M. Hillert, B. Sundman, *Acta Matall.* **24**, 731 (1976).

72. D. Fan, S.P. Chen, L-Q. Chen, *J. Mater. Res.* **14**, 1113 (1999).

73. K. Grönhagen, J. Ågren, *Acta Mater.* **55**, 955 (2007).

74. T.W. Heo, S. Bhattacharyya, L.-Q. Chen, *Acta Mater.* **59**, 7800 (2011).

75. Y. Dong, I.W. Chen, *J. Am. Ceram. Soc.* **101**, 1857 (2018).

76. R. Raj, *J. Eur. Ceram. Soc. 32*, 2293 (2012).

77. I.J. Hewitt, A.A. Lacey, R.I. Todd, *Math. Model Nat. Phenom.* **10**, 77 (2015).

78. Y. Du, A.J. Stevenson, D. Vernat, M. Diaz, D. Marinha, *J. Eur. Ceram. Soc.* **36**, 749 (2016).

79. K. Vanmeensel, A. Laptev, J. Hennicke, J. Vleugels, O. Van der Biest, *Acta Mater.* **53**, 4379 (2005).

80. X. Wang, S.R. Casolco, G. Xu, J.E. Garay, *Acta Mater.* **55**, 3611 (2017).

81. C. Wang, *et al.*, *Science* **368**, 521 (2020).

82. Y. Zhang, J.Nie, J.M. Chan, J. Luo, *Acta Mater.* **125**, 465 (2017).

83. W. Ji, B. Parker, S. Falco, J.Y. Zhang, Z.Y. Fu, R.I. Todd, *J. Eur. Ceram. Soc.* **37**, 2547 (2017).

84. W. Ji, J.Y. Zhang, W. Wang, Z.Y. Fu, R.I. Todd, *J. Eur. Ceram. Soc.* **40**, 5829 (2020).

Figures and Figure captions

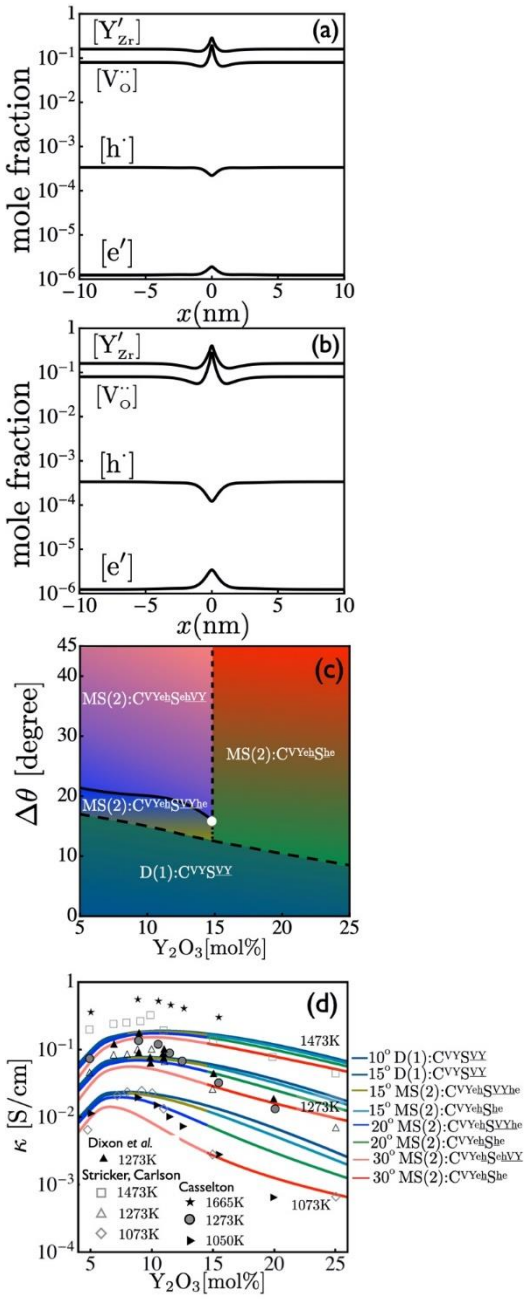

Figure 1. (a) Debye, (D)-type, interface for a small angle misorientation, $\Delta\theta = 15°$. (b) Mott–Schottky, (MS)-type, interface for a large angle misorientaion, $\Delta\theta = 30°$. (c) Grain-boundary phase diagram of YSZ at 2000 K, displaying different types of charged layers as a function of misorientation and dopant concentration. (d) Macroscopic total conductivity of the different grain-boundary types as a function of yttria.[30]

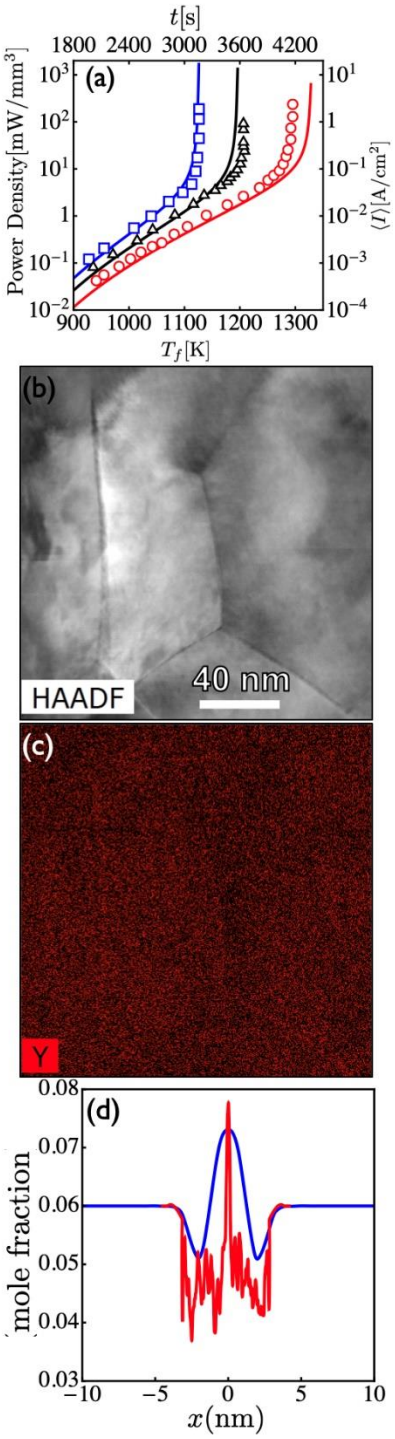

Figure 2. (a) Experimental and predicted macroscopic power density and average current density, as a function of furnace temperature and time, for 3YSZ samples, subjected to a constant heating rate of 10 K/min, for three applied electric fields: 60 V/cm (red), 90 V/cm (black), and 120 V/cm (blue). Symbols correspond the experimental results, as reported by Cologna and co-workers.[4] HAADF-STEM

image for flash sintered 3YSZ specimens of a grain boundary is shown in (b). The corresponding yttrium elemental mapping in (c). (d) Directly compares the yttrium profile (red) and phase-field prediction (blue) of the yttrium segregation spatial distribution in the vicinity of a particle-particle contact, for a tilt misorientation.[28]

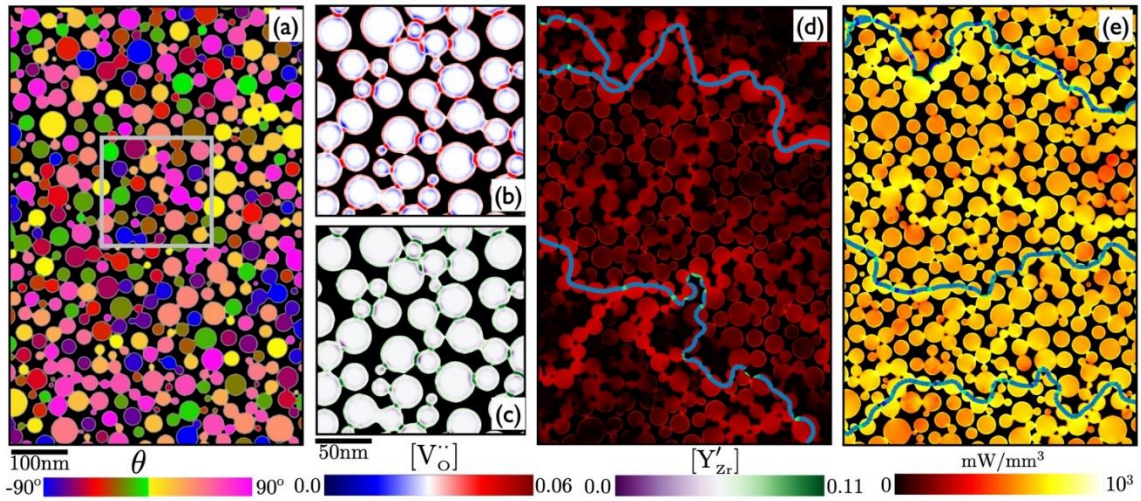

Figure 3. (a) A section of the computer-generated 3YSZ microstructure. (b) The oxygen vacancies distribution; (c) the yttrium distribution in the microstructural region highlighted (gray box) in (a). (d, e) Spatial distribution and percolative paths of Joule heating being generated at $T_f = 1000$ K and $T_f = 1300$ K.[28]

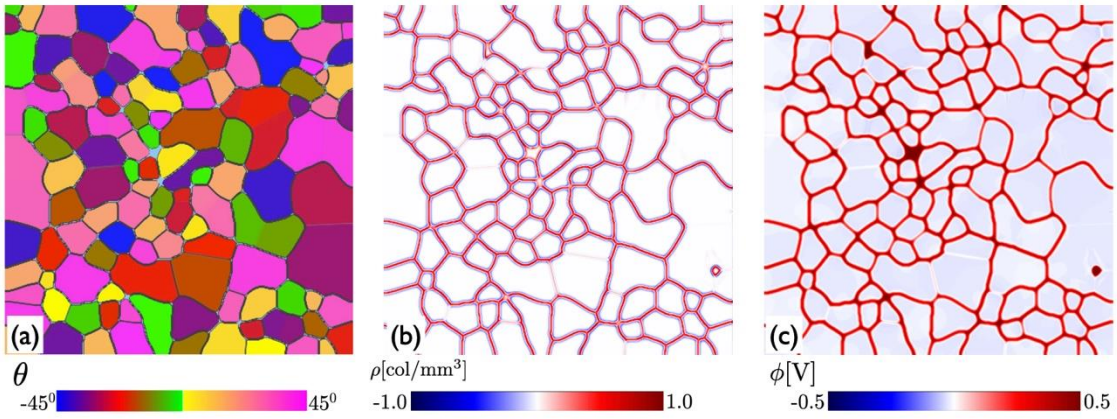

Figure 4. Simulated grain growth of 8YSZ at 2000 K. (a) Orientation field microstructure evolution. (b) Corresponding charge density. (c) Electrostatic potential distribution.[68,69]

K.S.N. Vikrant is a postdoctoral researcher at Oak Ridge National Laboratory (ORNL). He received his BTech degree in materials and metallurgical engineering from the Indian Institute of Technology Kanpur, India. Prior to joining ORNL, he was a postdoctoral researcher in the Materials Engineering Department at Purdue University, where he also earned his PhD degree. He research focuses on the formulation of variational models of charged interfaces in ionic ceramics for energy-storage and energy-conversion applications. He has published 17 peer-reviewed articles and holds one patent and seven copyrights. Vikrant can be reached by email at k.s.n.vikrant@gmail.com.

Xin Li Phuah is a a doctoral candidate at Purdue University. She earned her BS degree from Purdue University in 2017. Her research focuses on the processing and characterization of flash-sintered ceramics. Phuah can be reached by email at xphuah@purdue.edu.

Jarrod Lund is a doctoral candidate in materials engineering at Purdue University. He earned his BS degrees in mechanical engineering and mathematics at Brigham Young University. His research focuses on the data science of thermodynamic material properties, specializing in the accurate simulation and machine learning of electrochemically active materials. Lund can be reached by email at lund3@purdue.edu.

Han Wang is a postdoctoral researcher at Pacific Northwest National Laboratory. She received her BE degree in materials engineering from Nanchang University, China), her ME degree in materials engineering from Stevens Institute of Technology, and her PhD degree in materials engineering from Purdue University. Her research includes epitaxial growth and properties of transition-metal oxide thin films and characterization of functional materials. Wang can be reached by email at han.wang@pnnl.gov.

C. Stephen Hellberg is a research physicist at the US Naval Research Laboratory (NRL). He received his AB degree in physics from Princeton University and his PhD degree in physics from the University of Pennsylvania. He completed postdoctoral research at Florida State University and NRL. His research focuses on materials with strongly correlated electrons, quantum dots, defects in materials, quantum computation, and van der waals heterostructures. He has been an author or co-author in more than 75 publications and is a fellow of the American Physical Society. Hellberg can be reached by email at steve.hellberg@nrl.navy.mil.

Noam Bernstein is a research physicist at the US Naval Research Laboratory (NRL). He received his BS degree in applied physics and engineering and applied science from the California Institute of Technology, and his PhD degree in applied physics from Harvard University. He was a National Research Council postdoctoral research associate at NRL. His research includes many atomistic simulations, focusing on structural and mechanical properties and their applications to materials, including functional semiconductors, structural metals and ceramics, and battery materials. He is a fellow of the American Physical Society, has been included in more than 110 publications, and has 4400 citations and an h-index of 34. Bernstein can be reached by email at noam.bernstein@nrl.navy.mil.

Wolfgang Rheinheimer leads an Emmy-Noether Group funded by the German Research Foundation, Germany. He received his Diploma at the Karlsruhe Institute of Technology (KIT), Germany. He completed postdoctoral research at KIT, and was a visiting professor at Purdue University. His research focuses on microstructure evolution in ionic materials, and the segregation and processing aspects during sintering and grain growth and the resulting functional properties. Rheinheimer can be reached by email at w.rheinheimer@fz-juelich.de

Catherine M. Bishop is an associate professor in mechanical engineering and the Postgraduate Director of Studies, Mechanical Engineering Leader, Materials Cluster at the University of Canterbury, New Zealand. Bishop can be reached by email at catherine.bishop@canterbury.ac.nz.

Haiyan Wang is the Basil R. Turner Professor of Engineering in the School of Materials Engineering and School of Electrical and Computer Engineering at Purdue University. She specializes in nanostructured functional ceramics for multifunctional hybrid materials, microelectronics, optoelectronics, high-temperature superconductors, solid oxide fuel cells, plasmonics and photonics, ferroelectric and ferromagnetic applications, radiation-tolerant materials, and structural materials. She has published more than 530 journal articles (citation 19,000 times, H-index of 67) and presented more than 250 invited and contributed talks at various international conferences. Wang can be reached by email at hwang00@purdue.edu.

R. Edwin García is a professor in materials engineering at Purdue University. He received his BS degree in physics at the National University of Mexico, and his PhD degree in materials science and engineering at the Massachusetts Institute of Technology in 2003. He completed postdoctoral research at the National Institute of Standards and Technology. His research focuses on the design of materials and devices through the development of a fundamental understanding of the solid-state physics of the individual phases, their short- and long-range interactions, and their associated microstructural properties and time evolution. Garcia can be reached by email at redwing@purdue.edu.